Minkowski Functionals in Joint Galaxy Clustering & Weak Lensing Analyses

MINKOWSKI FUNCTIONALS IN JOINT GALAXY CLUSTERING & WEAK LENSING ANALYSES

Nisha Grewal[1]*, Joe Zuntz[1], Tilman Tröster[1], and Alexandra Amon[2]

[1]Institute for Astronomy, University of Edinburgh, Royal Observatory, Blackford Hill, Edinburgh, EH9 3HJ, UK
[2]Institute of Astronomy, University of Cambridge, Madingley Road, Cambridge, CB3 0HA, UK

Version August 23, 2022

ABSTRACT

We investigate the inclusion of clustering maps in a weak lensing Minkowski functional (MF) analysis of DES-like and LSST-like simulations to constrain cosmological parameters. The standard 3x2pt approach to lensing and clustering data uses two-point correlations as its primary statistic; MFs, morphological statistics describing the shape of matter fields, provide additional information for non-Gaussian fields. Previous analyses have studied MFs of lensing convergence maps; in this project we explore their simultaneous application to clustering maps. We employ a simplified linear galaxy bias model, and using a lognormal curved sky measurement and Monte Carlo Markov Chain (MCMC) sampling process for parameter inference, we find that MFs do not yield any information in the Ω_m – σ_8 plane not already generated by a 3x2pt analysis. However, we expect that MFs should improve constraining power when nonlinear baryonic and other small-scale effects are taken into account. As with a 3x2pt analysis, we find a significant improvement to constraints when adding clustering data to MF-only and MF+C_ℓ shear measurements, and strongly recommend future higher order statistics be measured from both convergence and clustering maps.

1. INTRODUCTION

Statistics measured from gravitational lensing have been effective in probing the growth of large-scale structure and the behaviour of gravity on cosmological scales. Ongoing surveys like the Dark Energy Survey[1] (DES; Flaugher 2005), Hyper Supreme-Cam[2] (HSC; Aihara et al. 2017) survey, and Kilo-Degree Survey[3] (KiDS; Kuijken et al. 2015) observe tens to hundreds of millions of galaxies. Covering 5000 deg², 1400 deg², and 1500 deg² respectively, these surveys construct detailed galaxy catalogs (Gatti et al. 2021b; Giblin et al. 2021; Aihara et al. 2022) and high resolution weak lensing maps (e.g. Jeffrey et al. 2021) and have extracted significant cosmological information from their data (Heymans et al. 2021; Miyatake et al. 2021; Abbott et al. 2022).

Cosmic shear is independent of galaxy bias and sensitive to the geometry and evolution of the Universe, making it particularly informative in the study of large scale structure (Hikage et al. 2019; Hamana et al. 2020; Asgari et al. 2021; Amon et al. 2022; Secco et al. 2022a). Using the ΛCDM model, which takes the assumption that the Universe comprises baryonic matter, cold dark matter, and dark energy, two-point statistics of weak lensing and galaxy clustering have been used successfully to constrain cosmological parameters that describe the model.

Measuring both convergence and clustering information using two-point statistics, such as correlation functions or the angular power spectra C_ℓ, has proven particularly effective, yielding high precision constraints on cosmological parameters Ω_m and σ_8 (Heymans et al. 2021; Miyatake et al. 2021; Abbott et al. 2022).

The two-point measurements described above encode all the information present in purely Gaussian random fields. In the non-Gaussian fields generated by nonlinear structure formation, however, other (higher-order) statistics can contain additional information. One example is peak statistics, which, when applied to weak lensing maps, can break degeneracies between cosmological parameters while remaining robust against systematic effects (e.g. Dietrich and Hartlap 2010; Kratochvil et al. 2010; Liu et al. 2015; Kacprzak et al. 2016; Shan et al. 2017; Martinet et al. 2018; Peel et al. 2018b; Ajani et al. 2020; Zürcher et al. 2022). Other higher order statistics of galaxy density, galaxy shear, and cosmic microwave background (CMB) lensing like three point correlation functions and bi-spectra (e.g. Takada and Jain 2003; Vafaei et al. 2010; Semboloni et al. 2011; Petri et al. 2013; Fu et al. 2014; Secco et al. 2022b) as well as moments (e.g. Van Waerbeke et al. 2013; Petri et al. 2015; Vicinanza et al. 2016; Chang et al. 2018; Peel et al. 2018a; Vicinanza et al. 2018; Gatti et al. 2020; Gatti et al. 2021a) are able to achieve even higher precision.

Many statistics, including these, are measured from maps generated from galaxy catalogues. Convergence maps, which are projected measures of mass along the line of sight, are derived from shear catalogues of source galaxies. Clustering maps, which show the number density of galaxies, are built from lens galaxy position catalogues and are complementary tracers of cosmic structure (Elvin-Poole et al. 2018). Clustering maps have a higher signal to noise ratio, enabling more detailed results (Jeffrey et al. 2021). However, clustering maps are only able to probe the distribution of galaxies, so galaxy bias must be modelled to relate this to the density of dark matter, which dominates the overall matter density (Abbott et al. 2022).

The morphological descriptors *Minkowski functionals* (MFs) are another higher-order statistic applicable in this context (Minkowski 1903). MFs are unbiased functional integrals over fields, have low variance, and have been applied previously to non-Gaussian convergence maps (Mecke et al. 1993; Kratochvil et al. 2012; Petri et al. 2013; Parroni et al. 2020), CMB data (e.g. Schmalzing and Gorski 1998, and references thereto), and 3D density fields from spectroscopic data (Hikage et al. 2003; Wiegand and Eisenstein 2017; Sullivan et al. 2019; Appleby et al. 2022). For a purely Gaussian field within a ΛCDM model, MFs and C_ℓ contain the same information for Ω_m and σ_8. Adding MFs to a single lensing field analysis has been shown to greatly improve constraints on cosmological parameters, and their angular-

scale dependence is particularly effective in separating primordial non-Gaussianities from gravity-induced non-Gaussianities (Munshi et al. 2011; Shirasaki et al. 2012; Vicinanza et al. 2019). Because they are sensitive to small-scale structure, MFs have strong constraining power. They have the potential to have additional resilience to some systematic uncertainties (Zürcher et al. 2021). Multiple MFs at different smoothing scales probe more information than a single set of MFs, and more analytical treatments like Hermite polynomials (Appleby et al. 2022) could extract more information as well.

In this paper, we investigate the effectiveness of the application of the first three MFs to multi-field simulations of both convergence and clustering maps, with a focus on forecasting potential constraining power using upcoming datasets. Future surveys will be even wider and deeper than current surveys, have the capabilities to build more informed weak lensing maps, and provide even more cosmological information. The Legacy Survey Space and Time (LSST) at the Vera C. Rubin Observatory[4] (LSST Science Collaboration et al. 2009; LSST Dark Energy Science Collaboration 2012) and the space telescopes Euclid[5] (Scaramella et al. 2021) and Nancy Grace Roman[6] (Spergel et al. 2015) will map nearly half the sky, and so enable dramatically strong constraints on the dark sector. The statistical approach we develop here can eventually be applied to such datasets.

In Section 2 we cover the theory of MFs and power spectra C_ℓ, in Section 3 we go over the process by which we use an MCMC to generate cosmological parameter posterior values, in Section 4 we show the constraints on cosmological parameters from various scenarios, and we conclude in Section 5.

2. FORMALISM/THEORY

2.1. Minkowski Functionals

Minkowski functionals are mathematical descriptors of the topology of continuous fields (Minkowski 1903; Zürcher et al. 2021). For 2D random fields, there are three functionals, quantifying area, perimeter, and mean curvature of an excursion set (the region of a field above a given threshold; Parroni et al. 2020). The first three MFs are defined as

$$V_0(\nu) = \frac{1}{A} \int_A \Theta(\alpha(\mathbf{x}) - \nu) d\phi d\theta, \qquad (1)$$

$$V_1(\nu) = \frac{1}{4A} \int_A \delta(\alpha(\mathbf{x}) - \nu) \sqrt{\alpha_\phi^2 + \alpha_\theta^2} d\phi d\theta, \qquad (2)$$

$$V_2(\nu) = \frac{1}{2\pi A} \int_A \delta(\alpha(\mathbf{x}) - \nu)$$
$$\left(\frac{2\alpha_\phi \alpha_\theta \alpha_{\phi\theta} - \alpha_\phi^2 \alpha_{\theta\theta} - \alpha_\theta^2 \alpha_{\phi\phi}}{\alpha_\phi^2 + \alpha_\theta^2} \right) d\phi d\theta, \qquad (3)$$

where $\mathbf{x}$ is the location in the field, ν is a chosen threshold, A is the total area of the map, ϕ and θ are polar

coordinates, $\alpha(\mathbf{x})$ is the field value in two dimensions, and α_ϕ, α_θ, $\alpha_{\phi\theta}$, $\alpha_{\theta\theta}$, and $\alpha_{\phi\phi}$ are derivatives of the field (Minkowski 1903; Petri et al. 2013). In Eq. (1) the Heaviside function Θ selects the field region above the threshold, whose area is calculated; Eq. (2) employs the Dirac delta function to select the perimeter of that region whose heights are at the same level as the threshold; similarly, Eq. (3) finds the curvature of the boundary, which also describes the connectivity of the field (Minkowski 1903). Since the fields we use are not normalised to have unit variance, the sensitivity of σ_8 comes from the overall amplitudes of V_1 and V_2.

Figure 1 and 2 illustrate the three MFs. The excursion sets in Figure 1 give rise to the three MFs plotted as a function of the threshold value in 2. If we visualize the original 2D map as a topographic height map, the excursion sets are the regions above a given altitude.

2.2. Power Spectra

We will compare the constraining power of MFs to the standard 2D power spectrum C_ℓ. The angular power spectrum C_ℓ^{xy} measures the scale-dependent structure of two fields x, y, which in this case are either weak lensing convergence or galaxy density. Assuming an isotropic system,

$$\langle a_{lm}^x, a_{l'm'}^{y*} \rangle = \delta_{\ell\ell'} \delta_{mm'} C_\ell^{xy}, \qquad (4)$$

where a_{lm} is the spherical harmonic transform of a field (Kaplinghat et al. 2002). We project a 3D field $X(\vec{\chi})$ via a weighting function $w_x(\chi)$ into the 2D field x (Bartelmann and Maturi 2016):

$$x(\vec{\theta}) = \int_0^{\chi_S} d\chi w_x(\chi) X(\vec{\theta}, \chi). \qquad (5)$$

Using Limber's approximation in a flat Universe, we can convert P_{XY}, the 3D (cross-)power spectrum of X, Y, into the 2D angular power spectrum of x, y:

$$C_\ell^{xy} = \int_0^{\chi_S} d\chi \frac{w_x(\chi) w_y(\chi)}{\chi^2} P_{XY} \left(\frac{\ell + \frac{1}{2}}{\chi}, z(\chi) \right), \qquad (6)$$

where ℓ is the scalar multipole, χ_S is the comoving distance to the source plane, χ is the comoving angular diameter distance, and w is a radial kernel function (Limber 1954; Bartelmann and Schneider 2001; Bartelmann and Maturi 2016; Abbott et al. 2022). The kernel function for convergence is given by

$$w_\kappa^j(\chi) = \frac{3\Omega_m H_0^2}{2} \int_\chi^{\chi_H} d\chi' n_s^j(\chi') \frac{\chi}{a(\chi)} \frac{\chi' - \chi}{\chi'}, \qquad (7)$$

where Ω_m is the present-day matter density parameter, H_0 is the Hubble parameter, χ_H is the comoving distance to the horizon, $n(\chi)$ is the source galaxy number density distribution, and $a(\chi)$ is the scale factor (Bartelmann and Schneider 2001). For clustering, the kernel function is simpler:

$$n(\chi) = n(z(\chi)) \frac{dz}{d\chi} \qquad (8)$$

(Elvin-Poole et al. 2018). We do not use cross-correlations of maps in our simulations (see Section 3.1.1), so the statistical structure of our power spectrum analysis does not fully replicate 3x2pt analysis.
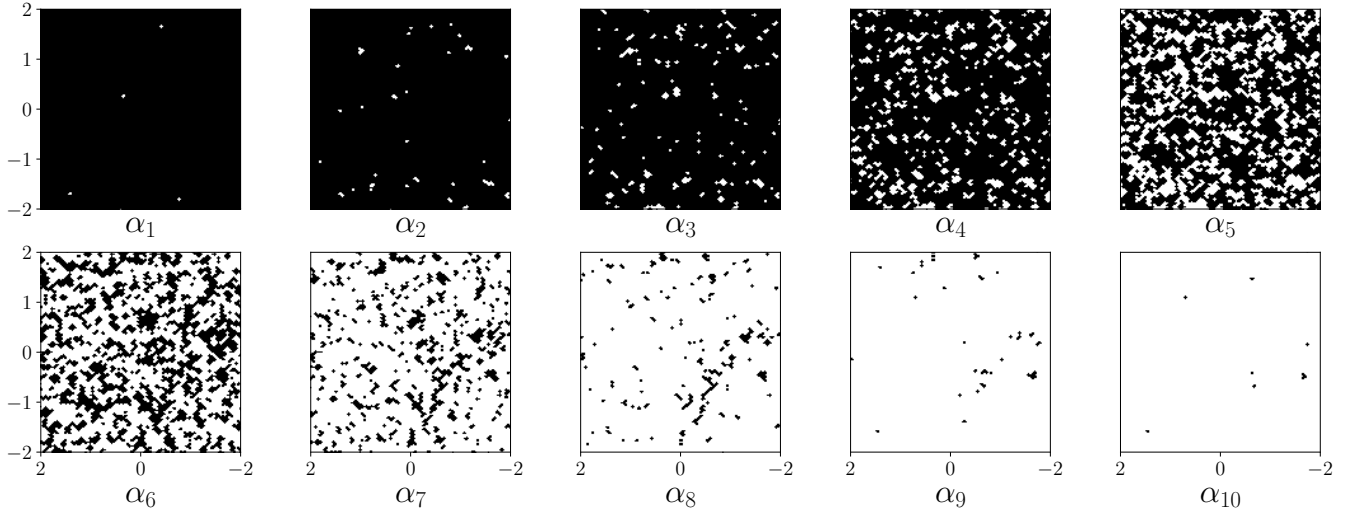
FIG. 1.— Excursion sets at 10 threshold values α of a simulated convergence map, where the regions under the threshold are marked in white and above in black.
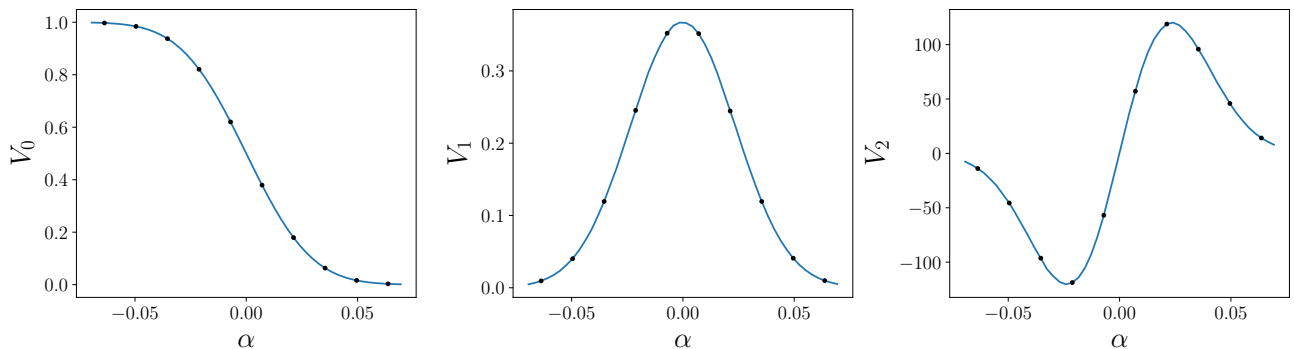

FIG. 2.— Sample of the first three MFs V_0, V_1, and V_2 calculated from a simulated weak lensing convergence map using fiducial $\Omega_{\rm m}$ and σ_8 values. Each black dot on the curve corresponds to an excursion set in Figure 1, and the three MFs on the y-axis describe the perimeter, area, and curvature of the mass distribution (Petri et al. 2013).

For Gaussian random fields, such as those in the nearly-homogeneous early Universe, C_ℓ contain all the information present (Coil 2013). While they are still useful for more general non-Gaussian late-time fields, they do not fully describe the statistics of such systems.

3. METHODOLOGY

In this paper we introduce the application of MFs to clustering maps. We compare the constraints on cosmological parameters from convergence maps, clustering maps, and a combination of the two. To measure these constraints, we explore the space of cosmological parameters with an MCMC process.

3.1. *Simulations*

In this work we generate curved sky lognormal simulations, which let us compute exact derivatives of the field. The lognormal sky simulations are relatively quick to evaluate and provide some degree of non-Gaussian signal. Our analysis has the flexibility to be measured from more sophisticated nonlinear, non-Gaussian simulations

in the future.

3.1.1. *Redshift*

To build these simulated maps we first start from DES Y6-like, LSST Y1-like, and LSST Y10-like tomographic number densities based on those in Zhang et al. (2021), which are shown in Figure 3 and Table 1. These $n(z)$ values are generated from an underlying true redshift distribution of the form $n_{\rm true}(z) \propto z^2 \exp{(z/z_0)}^a$, divided into equal density tomographic bins and then convolved with a Gaussian error distribution with width $\sigma(z) = (1 + z)\sigma_z$. Different values of the parameters a and σ_z and the number of bins and total density are used for our three different scenarios, DES Y6-like, LSST Y1-like, and LSST Y10-like, using the values given in Table 1 of Zhang et al. (2021).

3.1.2. *Map Simulation*

Next we use the Dark Energy Science Collaboration's (DESC; Abolfathi et al. 2021) Core Cosmology Library (CCL; Chisari et al. 2019) to predict theory values for
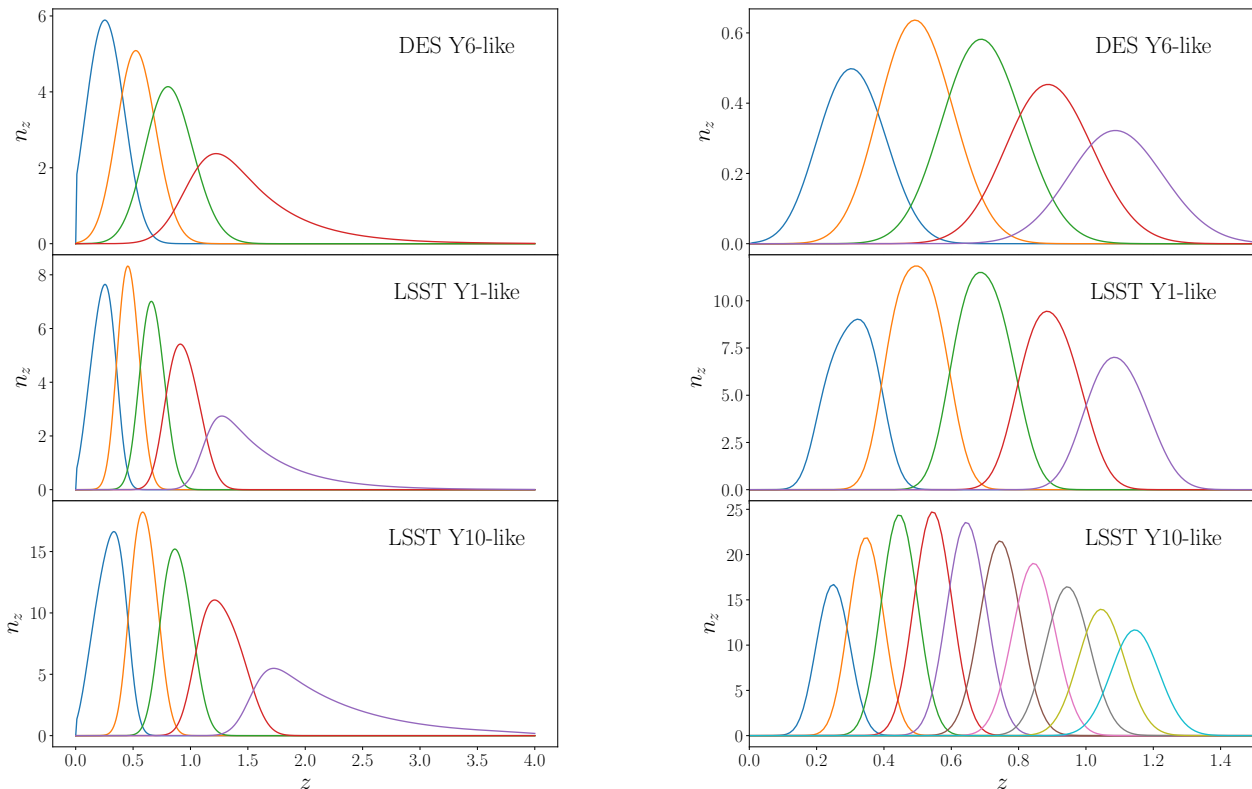
FIG. 3.— n_z redshift bins for DES Y6-like, LSST Y1-like, and LSST Y10-like (Hoyle et al. 2018; Zhang et al. 2021). Convergence distributions are displayed on the left, and clustering distributions are on the right.

	Bin 1	Bin 2	Bin 3	Bin 4	Bin 5	Bin 6	Bin 7	Bin 8	Bin 9	Bin 10
DES Y6-like	0.20-0.43	0.43-0.63	0.63-0.90	0.90-1.30						
LSST Y1-like	0.20-0.43	0.43-0.63	0.63-0.90	0.90-1.30						
LSST Y10-like	0.20-0.43	0.43-0.63	0.63-0.90	0.90-1.30						
DES Y6-like	1.17	1.28	1.41	1.55	1.69					
LSST Y1-like	1.17	1.28	1.41	1.55	1.69					
LSST Y10-like	1.13	1.19	1.25	1.32	1.38	1.45	1.51	1.58	1.65	1.72

TABLE 1
Convergence map redshift bins in the top three rows and clustering map galaxy bias values in the bottom three rows (Hoyle et al. 2018; Zhang et al. 2021).

the convergence and clustering power spectra C_ℓ. CCL takes the redshift distributions $n(z)$ and cosmological parameters and computes C_ℓ, which we pass with the $n(z)$ to the Full-sky Lognormal Astro-fields Simulation Kit (FLASK; Xavier et al. 2016) to simulate the convergence and clustering maps. FLASK generates continuous lognormal fields using spherical geometry (Xavier et al. 2016).

FLASK generates noisy clustering maps directly using the noise level we supply, and we manually add noise to the convergence maps it generates. In both cases we used Gaussian noise levels corresponding to the number densities in our scenarios. FLASK's mock fields, as with real fields, are more non-Gaussian for the clustering than for the lensing, since they are integrated over a narrower redshift kernel, and the code has specific corrections to allow a sensible joint analysis in this intermediate non-linear and non-Gaussian regime (Xavier et al. 2016).

We originally used more realistic Poisson noise in our clustering maps, but this caused problems when trying to fix the random seed (see below) in our simulations. Changing the power spectra that FLASK takes as input changes the cosmic variance and noise generated in the system. But while with Gaussian noise the same number

of random variates must be generated even as the mean levels change, this is not the case for Poisson noise. This means that for Poisson noise, a small change to input power spectra no longer creates a small change to the resulting maps, since the sequence of random noise values changes significantly[7].

3.1.3. *Simulation Inputs*

For this project, we use DES Y6-like, LSST Y1-like, and LSST Y10-like scenarios to find constraints on cosmological parameters. The cosmological parameter inputs we vary in the FLASK simulation are $\Omega_{\rm m}$ (total matter), σ_8 (amplitude of the matter power spectrum), $\Omega_{\rm b}$ (baryonic matter), H_0 (present-day rate of expansion of the Universe), and n_s (spectral index). We also vary linear galaxy bias values for the different lens bins. The fiducial values can be seen in Table 2.

Parameter	Fiducial	Min	Max
$\Omega_{\rm m}$	0.3	0.1	0.6
σ_8	0.8	0.3	1.2
Ω_b	0.048	0.047	0.049
H_0	0.7	0.5	0.9
n_s	0.96	0.9	1.1

TABLE 2
Fiducial values of cosmological parameters with the minimum and maximum values given to the MCMC generator.

To test the constraining power of adding clustering maps to the model, we use three sets of tomographic maps: convergence maps, clustering maps, and a combination of the two. Generating these simulations is slow, so we optimised a model that was informative while (relatively) efficient. We use $N_{\rm side} = 1024$ for the resolution parameter throughout, and follow Petri et al. (2013)'s choices for Gaussian smoothing θ_G and MF threshold count $N_{\rm bins}$, which can be seen in Table 3. While smoothing of 1 arcminute may be the most informative level, this is computationally taxing and essentially unsmoothed in our fields, thus subject to more noise. Going to smaller scales comes with other challenges, such as modelling uncertainties due to nonlinear galaxy bias and baryon feedback. Instead we use 5 arcminutes as the fiducial value, which is still informative at the $N_{\rm side} = 1024$ level.

We replicate DES Y6-like, LSST Y1-like, and LSST Y10-like scenarios in our simulations by applying the corresponding redshift bins, galaxy bias values, and sky fraction. The various scenarios are summarised in Table 3, and sample simulated convergence and clustering maps are shown in Figure 4. The "joint" case refers to both lensing and clustering.

3.2. *Observables*

To test the constraining power of MFs, we compare them to the standard C_ℓ analysis in cosmology. We compare the constraining power of the following three estimators: C_ℓ, MF, and the combination of C_ℓ and MF. We use the NaMaster[8] (Alonso et al. 2019) library to calculate

[7] An alternative solution would be to fix the mean of the noise field even as the signal changes.
[8] https://github.com/LSSTDESC/NaMaster

Statistic Type						
θ_G	$N_{\rm side}$	$N_{\rm bins}$	mask	n_z bins	MF/C_ℓ	Map Type
5	1024	10	0.125	DES Y6-like	C_ℓ	Joint
5	1024	10	0.44	LSST Y1-like	MF	Joint
5	1024	10	1	LSST Y10-like	C_ℓ+MF	Joint
Map Type						
θ_G	$N_{\rm side}$	$N_{\rm bins}$	mask	n_z bins	MF/C_ℓ	lens/clust
5	1024	10	0.125	DES Y6-like	Joint	Lensing
5	1024	10	0.44	LSST Y1-like	Joint	Clustering
5	1024	10	1	LSST Y10-like	Joint	Joint
Smoothing						
θ_G	$N_{\rm side}$	$N_{\rm bins}$	mask	n_z bins	MF/C_ℓ	lens/clust
1	1024	10	0.44	LSST Y1-like	Joint	Joint
5	1024	10	0.44	LSST Y1-like	Joint	Joint
15	1024	10	0.44	LSST Y1-like	Joint	Joint
Survey						
θ_G	$N_{\rm side}$	$N_{\rm bins}$	mask	n_z bins	MF/C_ℓ	lens/clust
5	1024	10	0.125	DES Y6-like	Joint	Joint
5	1024	10	0.44	LSST Y1-like	Joint	Joint
5	1024	10	0.44	LSST Y10-like	Joint	Joint

TABLE 3
Scenarios considered in this paper: comparing statistic type, map type, Gaussian smoothing θ_G at 1, 5, and 15 arcminutes; and survey model: DES Y6-like, LSST Y1-like, and LSST Y10-like.
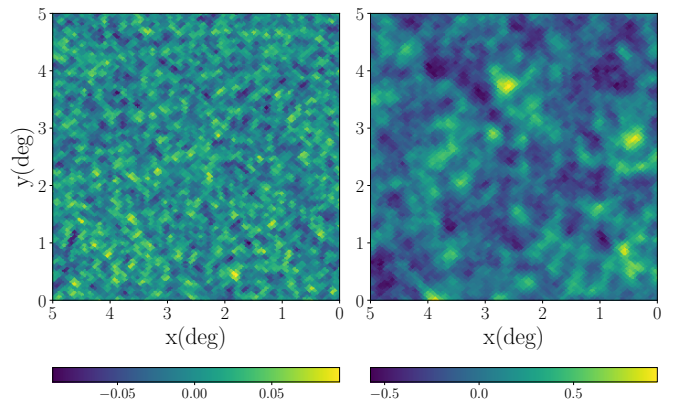

FIG. 4.— Small 5x5 degree flat sky piece of the curved sky clustering (left) and convergence (right) maps of redshift bin 4 at our fiducial cosmology, using $N_{\rm side} = 1024$ and 5 arcminutes of Gaussian smoothing. The convergence map colourbar shows convergence of each pixel, and the clustering map colourbar shows the galaxy over-density.

the full-sky auto-correlation convergence and density angular power spectra C_ℓ of the fields. We use a bandpower window function with 50 multipoles per bandpower. The maximum ℓ value we use is $\frac{3N_{\rm side}}{2}$, which is 1536 for $N_{\rm side}$ = 1024, which has a pixel size of 3.4 arcminutes. This means information below 7 arcminutes in the maps is smoothed out.

We give inputs for cosmological parameters, linear galaxy biases, pixel count, fraction of sky, and the amount of Gaussian smoothing applied to the map simulations.

We convert the integrals from Eq. (1), (2), and (3) to the sums in Eq. (9), (10), and (11), calculating the

values by taking a sum over the number of pixels N:

$$V_0(\nu_j) = \frac{1}{N} \sum_i \Theta(\alpha(\mathbf{x}_i) - \nu), \qquad (9)$$

$$V_1(\nu_j) = \frac{1}{4N} \sum_i \Delta(\alpha(\mathbf{x}_i) - \nu) \sqrt{\alpha_\phi^2 + \alpha_\theta^2}, \qquad (10)$$

$$V_2(\nu_j) = \frac{1}{2\pi N} \sum_i \Delta(\alpha(\mathbf{x}_i) - \nu)$$
$$\left(\frac{2\alpha_\phi \alpha_\theta \alpha_{\phi\theta} - \alpha_\phi^2 \alpha_{\theta\theta} - \alpha_\theta^2 \alpha_{\phi\phi}}{\alpha_\phi^2 + \alpha_\theta^2} \right), \quad (11)$$

where Δ is 1 when $\alpha(\mathbf{x}_i)$ is between ν_j and ν_{j+1} and 0 otherwise. The thresholds are evenly spaced from $\mu - 3\sigma$ to $\mu + 3\sigma$, where μ is the field value mean and σ is the field value standard deviation. We use HEALPix[9] to calculate first and second derivatives of the fields using a series of spherical harmonic transforms (Górski et al. 2005; Zonca et al. 2019).
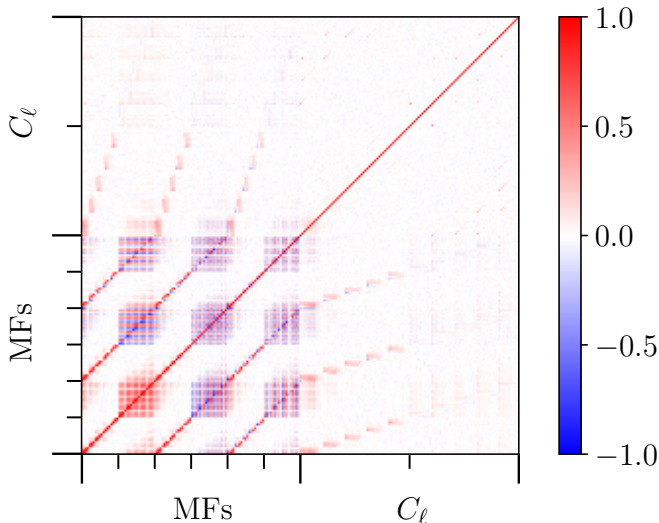
3.3. *Likelihood*

FIG. 5.— Correlation coefficient matrix of all observables for LSST Y1-like lensing + clustering analysis: 300 MFs and 300 C_ℓ. There is some correlation between the MFs and some between the MFs and C_ℓ. The ticks represent the range of the observables for the following statistics: V_0 clustering, V_0 lensing, V_1 clustering, V_1 lensing, V_2 clustering, V_2 lensing, C_ℓ clustering, C_ℓ lensing.

We follow a Bayesian procedure to measure our constraining power (Trotta 2017). To calculate likelihoods, we measure our observables on a suite of sky map realisations made using DES Y6-like fiducial values for cosmological parameters and biases. Once we have measured the C_ℓ and/or MFs on each clustering and/or convergence map set, we calculate the likelihood at other cosmologies with a Gaussian likelihood.

$$L \propto -0.5(\vec{x} - \vec{\mu})^t \mathbf{C}^{-1} (\vec{x} - \vec{\mu}), \qquad (12)$$

[9] http://healpix.sourceforge.net

where $\vec{\mu}$ represents mean observables over the suite of fiducial realizations, and $\mathbf{C}^{-1}$ is the inverse covariance matrix of the same suite. The simulated data point $\vec{x}$ is evaluated at other non-fiducial values of the input parameters. The calculations of μ and $\mathbf{C}^{-1}$ vary a random seed in map simulations and require a large number of simulations at the fiducial cosmology. To find the covariance of the statistics, we look at the correlation of the concatenation of the observables: MFs V_0, V_1, V_2, and/or the C_ℓ. The correlation matrix derived from this covariance is shown in Figure 5.

The number of fiducial realisations must be greater than or equal to the number of data points for the covariance matrix to be invertible. In our MF analysis, the number of data points is found by multiplying the number of thresholds used by three (the number of functionals) and the number of tomographic bins used, and the length of the C_ℓ is determined by the map resolution and binning. If there are too few fiducial simulations, the noise in the covariance overwhelms the signal and can cause errors in the constraining power calculation (Petri et al. 2013). One way to avoid this issue is to use more realisations, but this rapidly becomes time-consuming.

To make the correction for the finite number of simulations, we follow Petri et al. (2013) and make the Anderson (2003) adjustment to the inverse:

$$\langle \hat{\mathbf{C}}_*^{-1} \rangle = \frac{N}{N - p - 1} \Sigma^{-1}, \qquad (13)$$

where Σ^{-1} is the sample inverse covariance matrix, $\hat{\mathbf{C}}_*^{-1}$ is an estimator for the inverse covariance matrix, N is the number of realisations minus one (since we find the mean from the data), and p is the number of data points (Anderson 2003; Hartlap et al. 2006). With $N_{\rm side} = 1024$, there are 300 observables from C_ℓ and MFs each, so we have 600 data points total. We run the fiducial simulation up to 4000 times for each scenario.

3.4. *Sampling*

We use an MCMC to evaluate posterior values of cosmological parameters based on the output of the Gaussian log-likelihood function in Eq. (12). The cosmological parameter priors can be seen in Table 2 and the bias priors can be seen in Table 1. For this project we have wrapped the emcee ensemble sampler (Foreman-Mackey et al. 2013) via the cosmological parameter estimator framework CosmoSIS (Zuntz et al. 2015) to run and parallelise the likelihood calculation. We use 40 walkers to generate emcee chains with tens of thousands of samples. As the sampler takes a given number of iterations to explore the parameter space before it settles onto a stationary distribution, we truncate the first several thousand steps of the chains to eliminate the early 'burn-in' piece.

Since we are using a simulation to generate the maps and hence observables at each step of our chain, we would ideally marginalise over a large number of possible random seeds for the chain to find the mean observables for a given cosmology or else utilize a more sophisticated simulation-based inference framework (see, e.g. Cranner et al. 2020). Instead, we use the same random seed for every point in the chain, relying on the fact that with our configuration choices, the FLASK simulated fields are a smooth function of the cosmological parameters. Though

this process generates a noisy estimate of the model for a point in parameter space, it does yield a correct unnormalised likelihood, and the sampling acceptance criterion is correct.

Our DES Y6-like model has four redshift bins of source galaxies and five redshift bins of lens galaxies, LSST Y1-like has five redshift bins of source galaxies and five redshift bins of lens galaxies, and LSST Y10-like has five redshift bins of source galaxies and ten redshift bins of lens galaxies. We use only a simple linear model for galaxy bias, with the fiducial bias values calculated using

$$b_i = \frac{1}{D(\overline{z_i})}, \qquad (14)$$

where $D(\overline{z_i})$ is the growth factor as a function of redshifts at the fiducial cosmology.

3.5. *Masking*

Every survey comes with a sky mask, representing incomplete survey sky coverage, regions blocked by bright stars or other sources, and removals to keep systematic effects out of galaxy maps (Abbott et al. 2022). By limiting the available data, sky masks cause increased variance of fields and affect the estimated MFs values, since MFs are topological descriptors (Shirasaki et al. 2013). As such, MFs are only effective cosmological probes in simulations if masking is taken into account.

In this paper we use a simple polar cap sky fraction mask, in contrast to a more realistic analysis with complex small-scale mask features. For speed, we mask pixels after the simulations and derivatives are computed. However, taking derivatives of a field using harmonic transforms is only possible with a complete (unmasked) field. As such, in an analysis of real data, masked regions must be smoothed and convolved with field values around the mask. This must be carefully addressed in future analyses of real data.

4. RESULTS

Figure 6 shows a comparison of constraints on cosmological parameters from three sets of convergence and clustering statistics: MFs alone, C_ℓ alone, and a combination of MFs and C_ℓ. The C_ℓ contours are typical for a 3x2pt analysis; MFs alone show the same degeneracy direction at C_ℓ and show significant constraining power with standard deviations displayed in Table 4. Adding MFs to the 3x2pt analysis does not lead to significantly tighter constraints than C_ℓ alone, with only a 15% decrease in S_8 standard deviation, implying MFs and clustering C_ℓ contain largely the same information. The parameters Ω_8 and σ_8 separately are relatively poorly constrained.

Figure 7 compares constraints for the MF and C_ℓ analysis of convergence, clustering, and a combination of the two. As with standard 3x2pt analyses, adding clustering data to convergence adds significant constraining power to an MF plus C_ℓ analysis; the joint constraint is stronger than the sum of its parts, pointing to internal degeneracies being broken. The decreased error for the combined model can be compared with higher errors of the individual models in Table 4, demonstrating again the power of including clustering maps in the simulation.

Figure 8 shows constraints from the full convergence plus clustering, MF plus C_ℓ analysis for 1, 5, and 15 arcminute Gaussian smoothing. The resulting uncertainties are quantified in Table 4, and are not statistically different. This is largely as expected for given our N_{side} of 1024, which corresponds to 3.4 arcminute pixels, but the noticeable decrease in the S_8 constraint size for 15 arcminute smoothing may reflect the different trade-off for smoothing in MF analyses where noise suppression leads to better recovery of the excursion set boundary. With the tomographic number density that we are using here the measurements are noisy even over relatively large smoothing scales - we find the the noise contribution to the value dominates at all the three smoothing scales. Since MFs are higher order statistics, it is not possible to separate out the noise term, but the effect of this noise is included in both the theory and observed values in our MCMC, so does not matter too critically - it is the variation of the noise after that subtraction that affects the constraining power.

The trade-off between larger smoothing kernels to yield lower noise and smaller ones to retain small-scale power depends greatly on the details of the analysis and model. Understanding this relationship between scale and MF constraining power requires further study.

The constraints for the distributions of DES Y6-like, LSST Y1-like, and LSST Y10-like scenarios are shown in Table 4. As expected, surveys with more area, bins, and/or depth have stronger constraints.

Errors			
Analysis Type	Ω_m	σ_8	S_8
Cl	0.0040	0.0049	0.0014
MF	0.0132	0.0155	0.0019
Cl+MF	0.0045	0.0052	0.0012
Map Type	Ω_m	σ_8	S_8
Lensing	0.0090	0.0118	0.0029
Clustering	0.0101	0.0075	0.0147
Lensing+Clustering	0.0045	0.0052	0.0012
Smoothing (arcmin)	Ω_m	σ_8	S_8
1	0.0038	0.0045	0.0012
5	0.0045	0.0052	0.0012
15	0.0034	0.0044	0.0009
Survey (sky fraction)	Ω_m	σ_8	S_8
DES Y6-like (12.5%)	0.0053	0.0072	0.0017
LSST Y1-like (44%)	0.0045	0.0053	0.0012
LSST Y10-like (44%)	0.0006	0.0004	0.0006

TABLE 4
Errors on cosmological parameters for different scenarios.

5. CONCLUSION

In this paper we investigate the impact of including clustering measurements in analyses of Minkowski functionals combined with power spectra on cosmological constraints. Using simulated convergence and clustering maps, we measure the constraining power of the two statistics for DES Y6-like, LSST Y1-like, and LSST Y10-like surveys. While MFs have been previously proven to be useful in convergence map analyses, here we explore their application to photometric clustering maps for the first time. We compare analyses of varying measurement
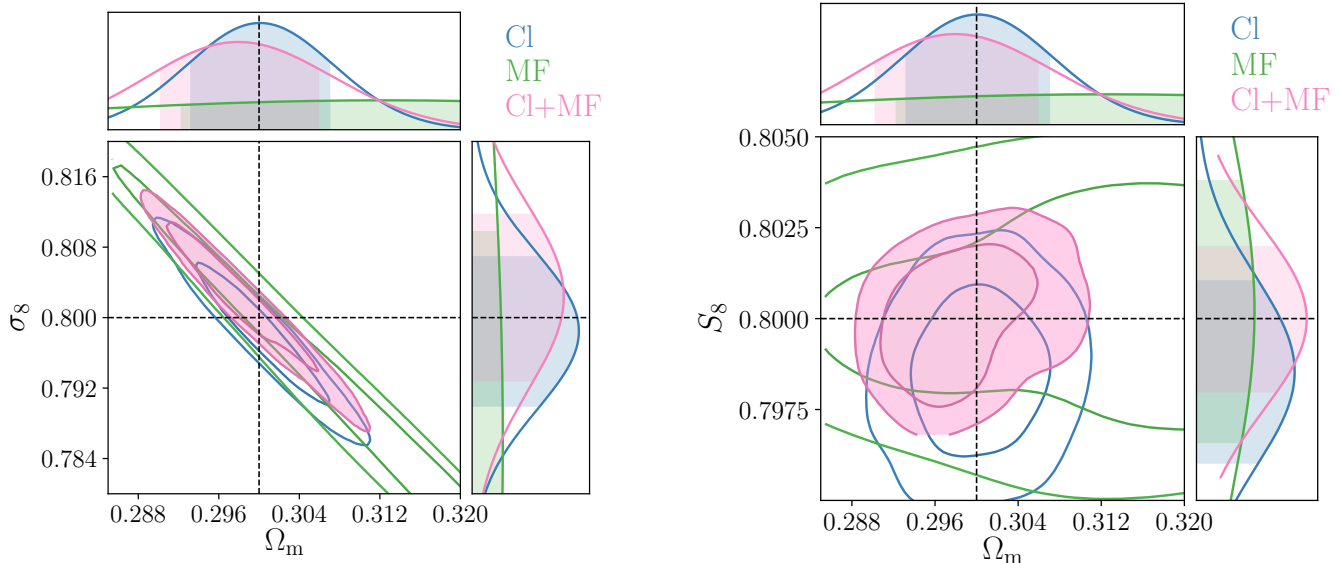
FIG. 6.— ΛCDM constraints for power spectra (blue), MFs (green), and joint analysis (pink) measured from convergence + clustering maps using LSST Y1-like redshift bins. Contours show 68% and 95% confidence levels. The left plot shows constraints on Ω_m and σ_8, and the right plot shows constraints on Ω_m and S_8. Adding MFs to the 3x2pt analysis does not lead to significantly tighter constraints than C_ℓ alone, implying MFs and clustering C_ℓ contain largely the same information.
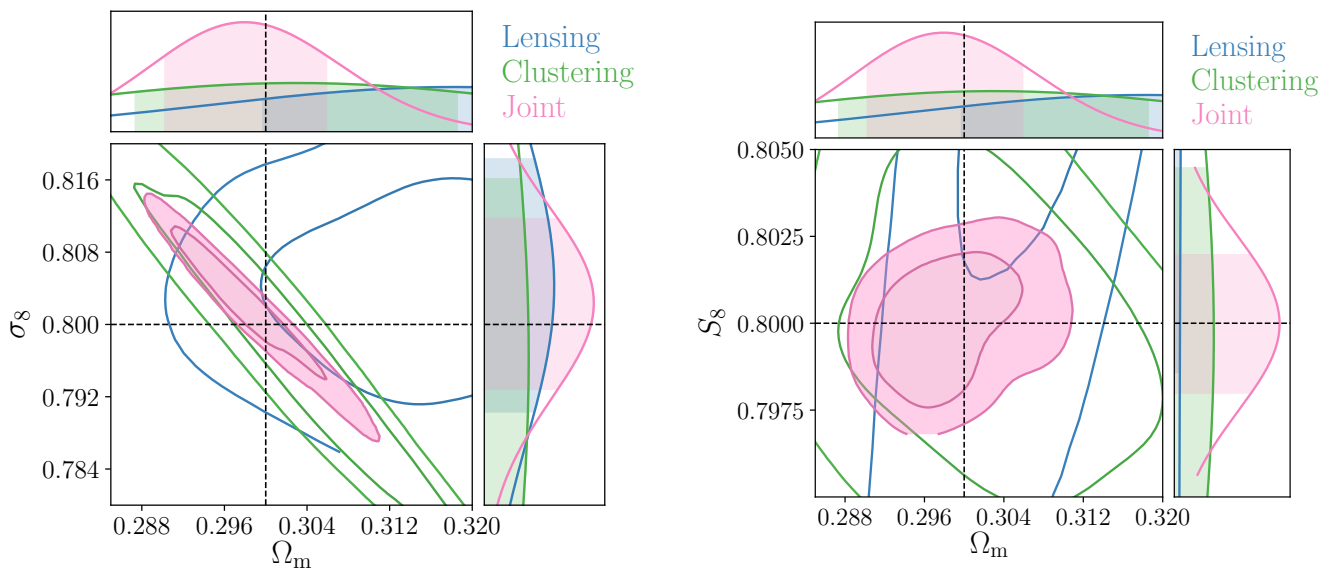

FIG. 7.— ΛCDM constraints for joint MF and C_ℓ statistics measured from convergence (green), clustering (blue), convergence and clustering (shaded in pink) maps using LSST Y1-like redshift bins. Contours show 68% and 95% confidence levels. The left plot shows constraints on Ω_m and σ_8, and the right plot shows constraints on Ω_m and S_8. As with standard 3x2pt analyses, adding clustering data to convergence adds significant constraining power to an MF plus C_ℓ analysis.

statistics, survey data properties, statistical power, and smoothing levels and present constraints on Ω_m, σ_8, and the better constrained S_8.

The MF measurements have the same S_8 degeneracy direction as power spectrum measurements, so we focus on this parameter when inspecting the impact of analysis type, map type, and smoothing amount, as it is generally more robust to analysis choices. We find that MFs probe similar cosmological information to clustering measurements in a 3x2pt analysis, and therefore the improvement on cosmological constraints for Ω_m, σ_8, and S_8 is limited, at least in our simplified lognormal map simula-

tion. An important limitation to our analysis, our use of only the auto-correlation C_ℓ, strengthens this conclusion, since the constraining power of the full 3x2pt analysis is even stronger than that presented here. Other limitations of our analysis, such as our omission of photo-z and shear-related nuisance parameters, are unlikely to change this conclusion, since they affect both MF and C_ℓ.

If there is value in including MFs in a 3x2pt analysis, it will perhaps become apparent only when we understand and incorporate small scale effects (i.e. baryons, intrinsic alignments, boost factors, mass reconstruction
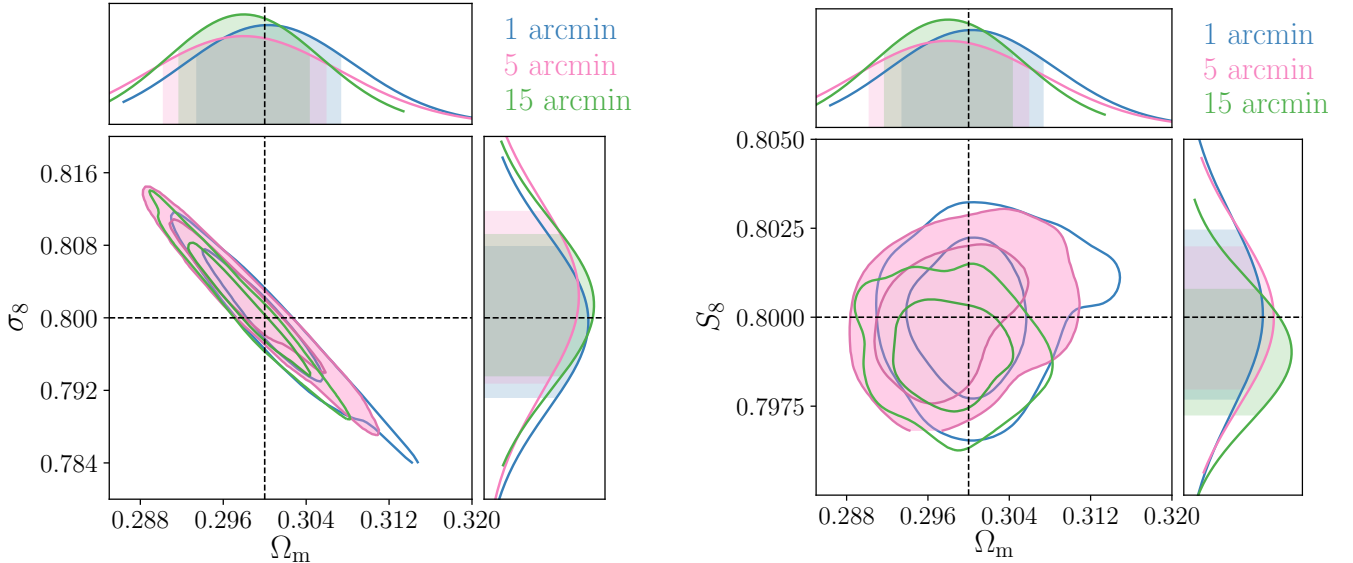
FIG. 8.— ΛCDM constraints for joint MF and C_ℓ statistics measured from LSST Y1-like redshift bins convergence and clustering maps for different Gaussian smoothing levels: 1 arcmin (blue), 5 arcmin (green), and 15 arcmin (pink). Contours show 68% and 95% confidence levels. The left plot shows constraints on Ω_m and σ_8, and the right plot shows constraints on Ω_m and S_8. There is not a statistically significant difference in constraining power between the smoothing levels.

on small scales, nonlinear galaxy bias) (e.g. Osato et al. 2021) combined with noise. That is, MFs are expected to have more potential on such nonlinear scales.

Similar to the standard 3x2pt case, in the C_ℓ+MF analysis we find that the addition of clustering measurements has a significant improvement on the constraints. For the LSST Y1-like case, we find an improvement of over 50% for all three cosmological parameters. Therefore, we recommend future higher order statistics be measured from both convergence and clustering maps.

In this project we use curved sky lognormal maps at Gaussian smoothing scales used by Petri et al. (2013) in convergence mapping, but the analysis has the flexibility to be measured from more sophisticated nonlinear, non-Gaussian data in the future. Our conclusions are significantly dependent on the specific form the non-Gaussian field takes, and so that the realism of the lognormal form of the field matters a great deal. On the intermediate scales that we use, previous research has shown that lognormal fields are a good approximation to real lensing fields Clerkin et al. (2016), so the general conclusions drawn here should be reasonable for clustering fields too.

An MF analysis that included all possible smoothing scales simultaneously would incorporate all the information available in a C_ℓ measurement Schmalzing and Gorski 1998, see e.g.. While such an analysis is not possible in practice, using a small number of different MF smoothing scales at the same is feasible and could improve the power of MFs.

The maps we use require high computational power, but since the primary constraining power of MFs will come at small scales, using full sky maps may not have been necessary for forecasts. We emphasise, however, that real measurements must consider curved sky effects.

As such, we make simplifications to the maps for computational efficiency. To usefully apply these statistics to real data one must take into account observing conditions, complex masking, baryon effects, and correlations between redshift bins. This is already true for current surveys like DES, HSC, and KiDS, but will be of heightened importance for upcoming efforts like Rubin, Euclid, and Roman. Masks present a particular challenge for many higher order statistics like MFs, since they increase the complexity of derivatives and other calculations.

This investigation motivates the use of MFs combined with C_ℓ in future analyses of convergence and clustering. Other potential applications for MFs include measuring them from shear maps, instead of convergence maps, or on combinations of fields. For practical data analysis, it is also critical to speed up or avoid the slow likelihood calculations used here, such as by using a faster implementation, an emulator, fitting function, neural network, or use likelihood-free inference. Building on the MF analysis in this work will improve and inform the statistical model used to constrain cosmological parameters when applied to future data.

6. ACKNOWLEDGMENTS

REFERENCES

T. M. C. Abbott, M. Aguena, A. Alarcon, S. Allam, O. Alves, A. Amon, F. Andrade-Oliveira, J. Annis, et al. Dark Energy Survey Year 3 results: Cosmological constraints from galaxy clustering and weak lensing. *Phys. Rev. D*, 105(2):023520, 2022. doi:10.1103/PhysRevD.105.023520.

B. Abolfathi, D. Alonso, R. Armstrong, E. Aubourg, H. Awan, Y. N. Babuji, F. E. Bauer, R. Bean, et al. The lsst desc dc2 simulated sky survey. *The Astrophysical Journal Supplement Series*, 253(1):31, Mar 2021. ISSN 1538-4365. doi:10.3847/1538-4365/abd62c.

H. Aihara, N. Arimoto, R. Armstrong, S. Arnouts, N. A. Bahcall, S. Bickerton, J. Bosch, K. Bundy, et al. The hyper suprime-cam ssp survey: Overview and survey design. *Publications of the Astronomical Society of Japan*, 70(SP1), Sep 2017. ISSN 2053-051X. doi:10.1093/pasj/psx066.

H. Aihara, Y. AlSayyad, M. Ando, R. Armstrong, J. Bosch, E. Egami, H. Furusawa, J. Furusawa, et al. Third data release of the hyper suprime-cam subaru strategic program. *Publications of the Astronomical Society of Japan*, 74(2):247–272, Feb 2022. doi:10.1093/pasj/psab122.

V. Ajani, A. Peel, V. Pettorino, J.-L. Starck, J. Liu, and Z. Li. Constraining neutrino masses with weak-lensing multiscale peak counts. *Physical Review D*, 102, 11 2020. doi:10.1103/PhysRevD.102.103531.

D. Alonso, J. Sanchez, and A. Slosar. A unified pseudo-cl framework. *Monthly Notices of the Royal Astronomical Society*, 484(3):4127–4151, Jan 2019. ISSN 1365-2966. doi:10.1093/mnras/stz093.

A. Amon, D. Gruen, M. A. Troxel, N. MacCrann, S. Dodelson, A. Choi, C. Doux, L. F. Secco, et al. Dark energy survey year 3 results: Cosmology from cosmic shear and robustness to data calibration. *Physical Review D*, 105(2), Jan 2022. doi:10.1103/physrevd.105.023514.

T. W. Anderson. *An introduction to multivariate statistical analysis.* John Wiley, 3rd edition, 2003.

S. Appleby, C. Park, P. Pranav, S. E. Hong, H. S. Hwang, J. Kim, and T. Buchert. Minkowski functionals of SDSS-III BOSS: Hints of possible anisotropy in the density field? *The Astrophysical Journal*, 928(2):108, mar 2022. doi:10.3847/1538-4357/ac562a.

M. Asgari, C.-A. Lin, B. Joachimi, B. Giblin, C. Heymans, H. Hildebrandt, A. Kannawadi, B. Stölzner, et al. Kids-1000 cosmology: Cosmic shear constraints and comparison between two point statistics. *Astronomy & Astrophysics*, 645:A104, Jan 2021. ISSN 1432-0746. doi:10.1051/0004-6361/202039070.

M. Bartelmann and M. Maturi. Weak gravitational lensing. 2016. doi:10.48550/ARXIV.1612.06535.

M. Bartelmann and P. Schneider. Weak gravitational lensing. *Physics Reports*, 340(4-5):291–472, Jan 2001. ISSN 0370-1573. doi:10.1016/s0370-1573(00)00082-x.

C. Chang, A. Pujol, B. Mawdsley, D. Bacon, J. Elvin-Poole, P. Melchior, A. Kovács, B. Jain, et al. Dark Energy Survey Year 1 results: curved-sky weak lensing mass map. *MNRAS*, 475(3): 3165–3190, April 2018. doi:10.1093/mnras/stx3363.

N. E. Chisari, D. Alonso, E. Krause, C. D. Leonard, P. Bull, J. Neveu, A. Villarreal, S. Singh, et al. Core cosmology library: Precision cosmological predictions for lsst. *The Astrophysical Journal Supplement Series*, 242(1):2, May 2019. ISSN 1538-4365. doi:10.3847/1538-4365/ab1658.

L. Clerkin, D. Kirk, M. Manera, O. Lahav, F. Abdalla, A. Amara, D. Bacon, C. Chang, et al. Testing the lognormality of the galaxy and weak lensing convergence distributions from dark energy survey maps. *Monthly Notices of the Royal Astronomical Society*, 466(2):1444–1461, aug 2016. doi:10.1093/mnras/stw2106.

A. L. Coil. The large-scale structure of the universe. *Planets, Stars and Stellar Systems*, page 387–421, 2013. doi:10.1007/978-94-007-5609-0˙8.

K. Cranmer, J. Brehmer, and G. Louppe. The frontier of simulation-based inference. *Proceedings of the National Academy of Sciences*, 117(48):30055–30062, 2020. doi:10.1073/pnas.1912789117.

J. P. Dietrich and J. Hartlap. Cosmology with the shear-peak statistics. *Monthly Notices of the Royal Astronomical Society*, 402(2):1049–1058, 02 2010. ISSN 0035-8711. doi:10.1111/j.1365-2966.2009.15948.x.

J. Elvin-Poole, M. Crocce, A. Ross, T. Giannantonio, E. Rozo, E. Rykoff, S. Avila, N. Banik, et al. Dark energy survey year 1 results: Galaxy clustering for combined probes. *Physical Review D*, 98(4), Aug 2018. ISSN 2470-0029. doi:10.1103/physrevd.98.042006.

B. Flaugher. The Dark Energy Survey. *International Journal of Modern Physics A*, 20(14):3121–3123, January 2005. doi:10.1142/S0217751X05025917.

D. Foreman-Mackey, D. W. Hogg, D. Lang, and J. Goodman. emcee: The MCMC Hammer. *PASP*, 125(925):306, March 2013. doi:10.1086/670067.

L. Fu, M. Kilbinger, T. Erben, C. Heymans, H. Hildebrandt, H. Hoekstra, T. D. Kitching, Y. Mellier, et al. CFHTLenS: cosmological constraints from a combination of cosmic shear two-point and three-point correlations. *MNRAS*, 441(3): 2725–2743, July 2014. doi:10.1093/mnras/stu754.

M. Gatti, C. Chang, O. Friedrich, B. Jain, D. Bacon, M. Crocce, J. DeRose, I. Ferrero, et al. Dark Energy Survey Year 3 results: cosmology with moments of weak lensing mass maps - validation on simulations. *MNRAS*, 498(3):4060–4087, November 2020. doi:10.1093/mnras/staa2680.

M. Gatti, B. Jain, C. Chang, M. Raveri, D. Zürcher, L. Secco, L. Whiteway, N. Jeffrey, et al. Dark Energy Survey Year 3 results: cosmology with moments of weak lensing mass maps. 10 2021a. doi:10.48550/ARXIV.2110.10141.

M. Gatti, E. Sheldon, A. Amon, M. Becker, M. Troxel, A. Choi, C. Doux, N. MacCrann, et al. Dark energy survey year 3 results: weak lensing shape catalogue. *Monthly Notices of the Royal Astronomical Society*, 504(3):4312–4336, Apr 2021b. ISSN 1365-2966. doi:10.1093/mnras/stab918.

B. Giblin, C. Heymans, M. Asgari, H. Hildebrandt, H. Hoekstra, B. Joachimi, A. Kannawadi, K. Kuijken, et al. Kids-1000 catalogue: Weak gravitational lensing shear measurements. *Astronomy & Astrophysics*, 645:A105, Jan 2021. ISSN 1432-0746. doi:10.1051/0004-6361/202038850.

K. M. Górski, E. Hivon, A. J. Banday, B. D. Wandelt, F. K. Hansen, M. Reinecke, and M. Bartelmann. HEALPix: A Framework for High-Resolution Discretization and Fast Analysis of Data Distributed on the Sphere. *ApJ*, 622:759–771, April 2005. doi:10.1086/427976.

T. Hamana, M. Shirasaki, S. Miyazaki, C. Hikage, M. Oguri, S. More, R. Armstrong, A. Leauthaud, et al. Cosmological constraints from cosmic shear two-point correlation functions with hsc survey first-year data. *Publications of the Astronomical Society of Japan*, 72(1), Feb 2020. ISSN 2053-051X. doi:10.1093/pasj/psz138.

J. Hartlap, P. Simon, and P. Schneider. Why your model parameter confidences might be too optimistic - unbiased estimation of the inverse covariance matrix. *Astronomy & Astrophysics*, 464(1):399–404, Dec 2006. ISSN 1432-0746. doi:10.1051/0004-6361:20066170.

C. Heymans, T. Tröster, M. Asgari, C. Blake, H. Hildebrandt, B. Joachimi, K. Kuijken, C.-A. Lin, et al. KiDS-1000 cosmology: Multi-probe weak gravitational lensing and spectroscopic galaxy clustering constraints. *Astronomy & Astrophysics*, 646:A140, Feb 2021. doi:10.1051/0004-6361/202039063.

C. Hikage, J. Schmalzing, T. Buchert, Y. Suto, I. Kayo, A. Taruya, M. S. Vogeley, F. Hoyle, J. R. Gott, and J. Brinkmann. Minkowski functionals of SDSS galaxies i : Analysis of excursion sets. *Publications of the Astronomical Society of Japan*, 55(5):911–931, oct 2003. doi:10.1093/pasj/55.5.911.

C. Hikage, M. Oguri, T. Hamana, S. More, R. Mandelbaum, M. Takada, F. Köhlinger, H. Miyatake, et al. Cosmology from cosmic shear power spectra with Subaru Hyper Suprime-Cam first-year data. *Publications of the Astronomical Society of Japan*, 71(2), 03 2019. ISSN 0004-6264. doi:10.1093/pasj/psz010. 43.

B. Hoyle, D. Gruen, G. M. Bernstein, M. M. Rau, J. De Vicente, W. G. Hartley, E. Gaztanaga, J. DeRose, et al. Dark energy survey year 1 results: redshift distributions of the weak-lensing source galaxies. *Monthly Notices of the Royal Astronomical Society*, 478(1):592–610, Apr 2018. ISSN 1365-2966. doi:10.1093/mnras/sty957.

N. Jeffrey, M. Gatti, C. Chang, L. Whiteway, U. Demirbozan, A. Kovacs, G. Pollina, D. Bacon, et al. Dark energy survey year 3 results: Curved-sky weak lensing mass map reconstruction. *Monthly Notices of the Royal Astronomical Society*, 505(3): 4626–4645, May 2021. ISSN 1365-2966. doi:10.1093/mnras/stab1495.

T. Kacprzak, D. Kirk, O. Friedrich, A. Amara, A. Refregier, L. Marian, J. P. Dietrich, E. Suchyta, et al. Cosmology constraints from shear peak statistics in Dark Energy Survey Science Verification data. *Monthly Notices of the Royal Astronomical Society*, 463(4):3653–3673, 08 2016. ISSN 0035-8711. doi:10.1093/mnras/stw2070.

M. Kaplinghat, L. Knox, and C. Skordis. Rapid calculation of theoretical cosmic microwave background angular power spectra. *The Astrophysical Journal*, 578(2):665–674, Oct 2002. ISSN 1538-4357. doi:10.1086/342656.

J. M. Kratochvil, Z. Haiman, and M. May. Probing cosmology with weak lensing peak counts. *Physical Review D*, 81(4), Feb 2010. ISSN 1550-2368. doi:10.1103/physrevd.81.043519.

J. M. Kratochvil, E. A. Lim, S. Wang, Z. Haiman, M. May, and K. Huffenberger. Probing cosmology with weak lensing minkowski functionals. *Physical Review D*, 85(10), May 2012. ISSN 1550-2368. doi:10.1103/physrevd.85.103513.

K. Kuijken, C. Heymans, H. Hildebrandt, R. Nakajima, T. Erben, J. T. A. de Jong, M. Viola, A. Choi, et al. Gravitational lensing analysis of the kilo-degree survey. *Monthly Notices of the Royal Astronomical Society*, 454(4):3500–3532, Oct 2015. ISSN 1365-2966. doi:10.1093/mnras/stv2140.

D. N. Limber. The Analysis of Counts of the Extragalactic Nebulae in Terms of a Fluctuating Density Field. II. *Astrophys. J.*, 119:655, 1954. doi:10.1086/145870.

J. Liu, A. Petri, Z. Haiman, L. Hui, J. M. Kratochvil, and M. May. Cosmology constraints from the weak lensing peak counts and the power spectrum in cfhtlens data. *Phys. Rev. D*, 91:063507, Mar 2015. doi:10.1103/PhysRevD.91.063507.

LSST Dark Energy Science Collaboration. Large synoptic survey telescope: Dark energy science collaboration. 2012. doi:10.48550/ARXIV.1211.0310.

LSST Science Collaboration, P. A. Abell, J. Allison, S. F. Anderson, J. R. Andrew, J. R. P. Angel, L. Armus, D. Arnett, S. J. Asztalos, et al. Lsst science book, version 2.0. 2009. doi:10.48550/ARXIV.0912.0201.

N. Martinet, P. Schneider, H. Hildebrandt, H. Shan, M. Asgari, J. P. Dietrich, J. Harnois-Déraps, T. Erben, et al. KiDS-450: cosmological constraints from weak-lensing peak statistics - II: Inference from shear peaks using N-body simulations. *MNRAS*, 474(1):712–730, February 2018. doi:10.1093/mnras/stx2793.

K. R. Mecke, T. Buchert, and H. Wagner. Robust morphological measures for large-scale structure in the universe. 1993. doi:10.48550/ARXIV.ASTRO-PH/9312028.

H. Minkowski. *Mathematische Annalen*, volume Volumen und Oberfläche. Dec 1903.

H. Miyatake et al. Cosmological inference from the emulator based halo model II: Joint analysis of galaxy-galaxy weak lensing and galaxy clustering from HSC-Y1 and SDSS. *Publications of the Astronomical Society of Japan*, 11 2021. doi:10.48550/ARXIV.2111.02419.

D. Munshi, J. Smidt, S. Joudaki, and P. Coles. The morphology of the thermal sunyaev–zel'dovich sky. *Monthly Notices of the Royal Astronomical Society*, 419(1):138–152, 12 2011. doi:10.1111/j.1365-2966.2011.19679.x.

K. Osato, J. Liu, and Z. Haiman. κtng: effect of baryonic processes on weak lensing with illustristng simulations. *Monthly Notices of the Royal Astronomical Society*, 502(4):5593–5602, Feb 2021. ISSN 1365-2966. doi:10.1093/mnras/stab395.

C. Parroni, V. F. Cardone, R. Maoli, and R. Scaramella. Going deep with minkowski functionals of convergence maps. *Astronomy & Astrophysics*, 633:A71, Jan 2020. ISSN 1432-0746. doi:10.1051/0004-6361/201935988.

A. Peel, V. Pettorino, C. Giocoli, J.-L. Starck, and M. Baldi. Breaking degeneracies in modified gravity with higher (than 2nd) order weak-lensing statistics. *A&A*, 619:A38, November 2018a. doi:10.1051/0004-6361/201833481.

A. Peel, V. Pettorino, C. Giocoli, J.-L. Starck, and M. Baldi. Breaking degeneracies in modified gravity with higher (than 2nd) order weak-lensing statistics. *A&A*, 619:A38, November 2018b. doi:10.1051/0004-6361/201833481.

A. Petri, Z. Haiman, L. Hui, M. May, and J. M. Kratochvil. Cosmology with minkowski functionals and moments of the weak lensing convergence field. *Physical Review D*, 88(12), Dec 2013. ISSN 1550-2368. doi:10.1103/physrevd.88.123002.

A. Petri, J. Liu, Z. Haiman, M. May, L. Hui, and J. M. Kratochvil. Emulating the CFHTLenS weak lensing data: Cosmological constraints from moments and Minkowski functionals. *Phys. Rev. D*, 91(10):103511, May 2015. doi:10.1103/PhysRevD.91.103511.

R. Scaramella, J. Amiaux, Y. Mellier, C. Burigana, C. S. Carvalho, J. C. Cuillandre, A. Da Silva, A. Derosa, et al. Euclid preparation: I. the euclid wide survey. 2021. doi:10.48550/ARXIV.2108.01201.

J. Schmalzing and K. M. Gorski. Minkowski functionals used in the morphological analysis of cosmic microwave background anisotropy maps. *Monthly Notices of the Royal Astronomical Society*, 297(2):355–365, jun 1998. doi:10.1046/j.1365-8711.1998.01467.x.

L. F. Secco, S. Samuroff, E. Krause, B. Jain, J. Blazek, M. Raveri, A. Campos, A. Amon, et al. Dark energy survey year 3 results: Cosmology from cosmic shear and robustness to modeling uncertainty. *Physical Review D*, 105(2), Jan 2022a. doi:10.1103/physrevd.105.023515.

L. F. Secco et al. Dark energy survey year 3 results: Three-point shear correlations and mass aperture moments. 1 2022b. doi:10.48550/ARXIV.2201.05227.

E. Semboloni, T. Schrabback, L. van Waerbeke, S. Vafaei, J. Hartlap, and S. Hilbert. Weak lensing from space: first cosmological constraints from three-point shear statistics. *MNRAS*, 410(1):143–160, January 2011. doi:10.1111/j.1365-2966.2010.17430.x.

H. Shan, X. Liu, H. Hildebrandt, C. Pan, N. Martinet, Z. Fan, P. Schneider, M. Asgari, et al. Kids-450: cosmological constraints from weak lensing peak statistics – i. inference from analytical prediction of high signal-to-noise ratio convergence peaks. *Monthly Notices of the Royal Astronomical Society*, 474(1):1116–1134, Nov 2017. ISSN 1365-2966. doi:10.1093/mnras/stx2837.

M. Shirasaki, N. Yoshida, T. Hamana, and T. Nishimichi. Probing primordial non-gaussianity with weak-lensing minkowski functionals. *The Astrophysical Journal*, 760(1):45, Nov 2012. ISSN 1538-4357. doi:10.1088/0004-637x/760/1/45.

M. Shirasaki, N. Yoshida, and T. Hamana. Effect of mask regions on weak lensing statistics. *The Astrophysical Journal*, 774(2):111, Aug 2013. ISSN 1538-4357. doi:10.1088/0004-637x/774/2/111.

D. Spergel, N. Gehrels, C. Baltay, D. Bennett, J. Breckinridge, M. Donahue, A. Dressler, B. S. Gaudi, et al. Wide-field infrared survey telescope-astrophysics focused telescope assets wfirst-afta 2015 report. 2015. doi:10.48550/ARXIV.1503.03757.

J. M. Sullivan, A. Wiegand, and D. J. Eisenstein. The clustering of galaxies in the SDSS-III Baryon Oscillation Spectroscopic Survey: evolution of higher-order correlations demonstrated with Minkowski functionals. *Monthly Notices of the Royal Astronomical Society*, 485(2):1708–1719, 02 2019. ISSN 0035-8711. doi:10.1093/mnras/stz498.

M. Takada and B. Jain. Three-point correlations in weak lensing surveys: model predictions and applications. *MNRAS*, 344(3):857–886, September 2003. doi:10.1046/j.1365-8711.2003.06868.x.

R. Trotta. Bayesian methods in cosmology. 2017. doi:10.48550/ARXIV.1701.01467.

S. Vafaei, T. Lu, L. van Waerbeke, E. Semboloni, C. Heymans, and U.-L. Pen. Breaking the degeneracy: Optimal use of three-point weak lensing statistics. *Astroparticle Physics*, 32(6):340–351, 2010. ISSN 0927-6505. doi:https://doi.org/10.1016/j.astropartphys.2009.10.003.

L. Van Waerbeke, J. Benjamin, T. Erben, C. Heymans, H. Hildebrandt, H. Hoekstra, T. D. Kitching, Y. Mellier, et al. CFHTLenS: mapping the large-scale structure with gravitational lensing. *MNRAS*, 433(4):3373–3388, August 2013. doi:10.1093/mnras/stt971.

M. Vicinanza, V. F. Cardone, R. Maoli, R. Scaramella, and X. Er. Higher order moments of lensing convergence - I. Estimate from simulations. 6 2016. doi:10.48550/ARXIV.1606.03892.

M. Vicinanza, V. F. Cardone, R. Maoli, R. Scaramella, and X. Er. Increasing the lensing figure of merit through higher order convergence moments. *Phys. Rev. D*, 97(2):023519, January 2018. doi:10.1103/PhysRevD.97.023519.

M. Vicinanza, V. F. Cardone, R. Maoli, R. Scaramella, X. Er, and I. Tereno. Minkowski functionals of convergence maps and the lensing figure of merit. *Physical Review D*, 99(4), Feb 2019. ISSN 2470-0029. doi:10.1103/physrevd.99.043534.

A. Wiegand and D. J. Eisenstein. The clustering of galaxies in the SDSS-III baryon oscillation spectroscopic survey: higher order correlations revealed by germ–grain minkowski functionals. *Monthly Notices of the Royal Astronomical Society*, 467(3):3361–3378, Feb 2017. doi:10.1093/mnras/stx292.

H. S. Xavier, F. B. Abdalla, and B. Joachimi. Improving lognormal models for cosmological fields. *Monthly Notices of the Royal Astronomical Society*, 459(4):3693–3710, Apr 2016. ISSN 1365-2966. doi:10.1093/mnras/stw874.

Z. Zhang, C. Chang, P. Larsen, L. F. Secco, J. Zuntz, and the LSST Dark Energy Science Collaboration. Transitioning from Stage-III to Stage-IV: Cosmology from galaxy×CMB lensing and shear×CMB lensing. 2021. doi:10.48550/ARXIV.2111.04917.

A. Zonca, L. Singer, D. Lenz, M. Reinecke, C. Rosset, E. Hivon, and K. Gorski. healpy: equal area pixelization and spherical harmonics transforms for data on the sphere in python. *Journal of Open Source Software*, 4(35):1298, March 2019. doi:10.21105/joss.01298.

J. Zuntz et al. Cosmosis: Modular cosmological parameter estimation. *Astronomy and Computing*, 12:45–59, Sep 2015. ISSN 2213-1337. doi:10.1016/j.ascom.2015.05.005.

D. Zürcher, J. Fluri, R. Sgier, T. Kacprzak, M. Gatti, C. Doux, L. Whiteway, A. Refregier, et al. Dark energy survey year 3 results: Cosmology with peaks using an emulator approach. *Monthly Notices of the Royal Astronomical Society*, 511(2): 2075–2104, Jan 2022. doi:10.1093/mnras/stac078.

D. Zürcher, J. Fluri, R. Sgier, T. Kacprzak, and A. Refregier. Cosmological forecast for non-gaussian statistics in large-scale weak lensing surveys. *Journal of Cosmology and Astroparticle Physics*, 2021(01):028–028, Jan 2021. doi:10.1088/1475-7516/2021/01/028.